




# Heterogeneous 3D Morphological Evolution of Ni Microparticles in Molten Salts: Visualized by *Operando* Synchrotron X-ray Nano-tomography

XIAOYANG LIU,<sup>1</sup> ARTHUR RONNE,<sup>1</sup> LIN-CHIEH YU,<sup>1</sup>  
PHILLIP HALSTENBERG,<sup>2,3</sup> XIANGHUI XIAO,<sup>4</sup> WAH-KEAT LEE,<sup>4</sup>  
SHENG DAI,<sup>2,3</sup> MINGYUAN GE,<sup>4</sup> and YU-CHEN KAREN CHEN-  
WIEGART <sup>1,4,5</sup>

1.—Department of Materials Science and Chemical Engineering, Stony Brook University, Stony Brook, NY, USA. 2.—Department of Chemistry, University of Tennessee, Knoxville, TN, USA. 3.—Chemical Sciences Division, Oak Ridge National Laboratory, Oak Ridge, TN, USA. 4.—National Synchrotron Light Source II (NSLS-II), Brookhaven National Laboratory, Upton, NY, USA. 5.—e-mail: Karen.Chen-Wiegart@stonybrook.edu

Ni-based superalloys are promising materials for high-temperature molten salt (MS) energy generation and storage. Studying morphological and chemical evolution of pure Ni in MS provides fundamental knowledge for MS technologies and corrosion mitigation. Here, real-time 3D morphological changes of Ni microparticles in molten KCl-MgCl<sub>2</sub> were studied by *operando* synchrotron X-ray nano-tomography at 700°C. Rapid Ni particle agglomeration occurred, without significant chemical reactions, such as oxide or chloride formation. The morphological growth evolved differently from classical coarsening or sintering behaviors and occurred nonuniformly, with other regions showing slight dissolution of Ni. Ni nanoparticles were found to be dispersed in many areas of the samples, either from microparticle dissolution or other radiation-induced nanoparticle formation mechanisms. This study discusses important factors, i.e., thermal gradient, amounts of salt and metals, and radiation effect, that influence morphological changes of materials in MS, critical for fundamental understanding of material–MS interactions as well as for practical applications.

## INTRODUCTION

Molten salts are effective high-temperature heat transfer fluids and thermal storage media for a wide range of energy generation and storage facilities,<sup>1–3</sup> including concentrated solar power plants<sup>4–9</sup> and high-temperature batteries.<sup>10–13</sup> Molten salt reactors (MSRs), which use molten halide salt as the fuel carrier and heat transfer fluid, are prominent candidates for safer next-generation nuclear power plants.<sup>14–16</sup> Molten salt has also been used as an effective synthesis agent for inorganic nanomaterials<sup>17</sup> and two-dimensional materials.<sup>18,19</sup>

Consequently, understanding how materials interact with molten salts is an essential priority, and it is especially challenging to study such liquid/solid interfacial phenomena due to their complex environment and heterogeneous nature. For instance, corrosion has been recognized as one of the major challenges in molten salt technologies, with a range of fundamental and technical questions still unresolved.<sup>20–23</sup> The morphological evolution of materials in molten salts, including corrosion, involves the interplay between interfacial phenomena and long-range mass transport. The interfacial phenomena involve the electrochemical charge–transfer process at the metal–salt interface and the surface diffusion of metal atoms. The long-range mass transport could be in both the solid and liquid phases,

(Received August 31, 2022; accepted January 16, 2023;  
published online February 21, 2023)

including intergranular or bulk diffusion in the alloy, and oxidant or corrosion product diffusion in the molten salt. Providing fundamental insights regarding the processes including mass transport (surface and long-range diffusion, as well as convection) and charge transfer (chemical/electrochemical reactions) is a path towards revealing how the basic transport and reaction processes govern structural changes of materials in molten salts.

Considering the variable working environments in a molten salt reactor, the underlying mechanisms of molten salt–material reactions are complicated, including factors such as impurities due to the hygroscopic nature of the salt,<sup>24</sup> irradiation effects,<sup>25</sup> grow-in of fission products,<sup>26</sup> and temperature variations.<sup>27</sup> As a result, the molten salt and the contacted alloys may undergo chemical, morphological, and structural changes that significantly affect their properties and functions. Fundamentally, it is important to understand the individual processes involved in molten salt–alloy interactions.

In the gamut of morphological evolution phenomena at elevated temperatures, coarsening is an important factor influencing the morphological evolution of materials at high temperatures. Coarsening is an increase in characteristic length scale during microstructural evolution. The driving force for coarsening is minimization of the total interfacial energy.<sup>28</sup> Coarsening is also known as Ostwald ripening or competitive growth, is commonly observed in heterogeneous systems consisting of particles dispersed in a matrix, and occurs when large particles grow at the expense of small particle shrinkage.<sup>29</sup> Coarsening has been observed in molten salt dealloying with porous structures,<sup>30–32</sup> but it has yet to be studied extensively in molten salt media. Coarsening phenomena can be more broadly applied to a wider range of systems with different morphologies: the growth of pores and ligaments in bicontinuous nanoporous structures created by dealloying is one example,<sup>33–36</sup> this includes coarsening in molten salt media.

An important point is the differentiation between coarsening and densification for porous materials. Coarsening refers to an increase in dimension without changing the volume ratio between the solid phase and the pore phase, and thus not changing the porosity. In a bicontinuous system, it is typically achieved by surface diffusion, where materials are rearranged along the surface without affecting the porosity. However, densification, which involves bulk diffusion (also known as lattice diffusion) to reduce the porosity, can accompany coarsening and occurs in materials that are subjected to a high-temperature environment, as also observed in materials dealloyed by molten salt.<sup>30</sup>

X-ray nano-tomography is an effective tool to provide direct 3D visualization of a wide range of materials. With synchrotron full-field imaging techniques, such as transmission X-ray microscopy (TXM), rapid data acquisition and high data quality

provide the ability not only to capture the morphological evolution of the system but also to quantify their kinetics (pathways and rates).<sup>37–41</sup> For instance, several recent reports from our group have analyzed the morphological evolution of Ni-20Cr in molten KCl-MgCl<sub>2</sub> salts under different conditions.<sup>30,42</sup> The concurrent coarsening phenomena, during dealloying in particular, were analyzed in detail with a Ni-20Cr microwire.<sup>30</sup> TXM nano-tomography has also been used to quantify the coarsening mechanism of Ni in solid-oxide fuel cells,<sup>43–45</sup> as well as bicontinuous nanoporous gold.<sup>33,46</sup> Combined with the energy tunability available at a synchrotron source, spectroscopic imaging with TXM can provide spatially-resolved chemical information, also known as X-ray absorption near-edge structure (XANES) imaging and XANES tomography.<sup>47,48</sup>

This work studies the complicated behaviors of Ni, including coarsening, dissolution, and nanoparticle formation in molten salt, by directly capturing the 3D morphological evolution of Ni microparticles in molten salts with X-ray nano-tomography. The work is motivated by the need to know how to manage the aggregation and deposition of particulate materials in molten salt reactors and concentrated solar power plants, for the assurance of safety and reliability. Ni is a major component of the alloys used to construct salt loops in these systems, and various corrosion processes transfer oxidized and metallic Ni from the alloy to the salt phase, where radiation effects can re-reduce the oxidized Ni.<sup>49</sup> Additional morphological evolution characteristics have been observed, such as the presence of many smaller, well-dispersed Ni particles at sub-micron to nanometer scales. The heterogeneous morphological evolution due to the complex environment involving local salt/metal concentration variation, high temperature and X-ray radiation is discussed. Nanoparticle formation has been observed under the influence of chemical, radiolytic, or corrosive conditions for applications in nuclear reactors,<sup>49</sup> which is consistent with the observations of this study. Overall, this work serves as a step towards understanding the complex coupling between the different kinetics steps in the corrosion process, and how they determine the morphological changes of materials in a molten salt environment. Ongoing efforts in experiments, theoretical analysis, and computational modeling are critically needed to provide more detailed 3D morphological and chemical quantification and prediction in this research area.

## METHODS

### Sample Preparation

The MgCl<sub>2</sub> used in this study was purified following the method established from previous work,<sup>30</sup> then mixed with KCl (purchased as 99.999% Suprapur reagent grade) in a 50:50 molar

ratio. Ni powder (purity 99.5%, 1  $\mu\text{m}$ ; US Research Nanomaterials) was purchased and stored in a glovebox. Quartz capillaries (Charles Supper) with 0.1-, 0.3- and 0.5-mm diameters and 10- $\mu\text{m}$  wall thickness were baked in an oven (CASCADE TEK) at  $\sim 120^\circ\text{C}$  overnight to remove any surface moisture that may have been present and immediately transferred into an Ar-filled glovebox. The 0.1-mm capillaries were open-ended on both sides, while the 0.3- and 0.5-mm capillaries had one open funnel side and one closed tip side. Two different types of samples were prepared. For the first type, the ground powder of 5 wt% Ni mixed with KCl-MgCl<sub>2</sub> (50:50 mol%) was added into the 0.3-mm quartz capillary from the funnel side. Then, this capillary containing the Ni and salt powder was placed into a 0.5-mm quartz capillary. For the second type, the Ni powders were added into the 0.1-mm quartz capillary. The ground KCl-MgCl<sub>2</sub> (50:50 mol%) salt mixture was heated in a quartz boat in the glovebox at  $\sim 650^\circ\text{C}$  to a molten state. Then, the molten salt was drawn up into the capillary containing Ni powder, using a syringe connected by a tube, through the open tip within several seconds. The molten salt immediately solidified in the capillary, which was at room temperature. The capillary with the Ni powders and solidified salt mixture was then placed into a 0.5 mm capillary.

For both types of the samples, the 0.5-mm capillaries were then sealed with a small bead of epoxy at the funnel opening of the funnel end to ensure the Ar environment was preserved in the double-capillary assembly during the sample transfer. The epoxy was not in contact with the Ni or salt, which remained at the tip end of the capillary. After the epoxy was cured in the glovebox, the sample was transferred from the glovebox and immediately flame-sealed using a miniature benchtop hydrogen torch system (Rio Grande). The flame-sealed double-capillary sample assembly was then attached to an alumina rod (ID: 0.02"; McMaster-Carr) and mounted on a kinematic mount (TXM sample holder) using a high-temperature epoxy (RESBOND).

### In situ Synchrotron X-ray Nano-tomography Measurement

The in situ X-ray nano-tomography experiments were conducted at the Full Field X-ray Imaging beamline (FXI, 18-ID) at the Brookhaven National Laboratory National Synchrotron Light Source-II.<sup>50</sup> The sample was heated by a miniature furnace<sup>51</sup> integrated with the TXM endstation at FXI. The double-capillary sample containing Ni powder immersed in molten salt was heated to  $700^\circ\text{C}$  with a ramp rate of  $50^\circ\text{C}/\text{min}$ . The X-ray incident energy used was 9.8 keV, which provides a sufficient transmission signal and good contrast for the Ni

particles. The image was captured by a lens-coupled charge-coupled device detector ( $2560 \times 2160$  pixels, horizontal  $\times$  vertical) with 6.5- $\mu\text{m}$  pixel size, and camera binning was  $2 \times 2$  during the experiment. The magnification of the microscope was  $\times 300$ . Thus, the effective pixel size of the image was 43.34 nm. For all tomographic measurements, the exposure time was 40 ms per projection with 360 projections, which resulted in an acquisition time of less than 1 min per nano-tomogram.

Two in situ heating experiments (Fig. 1) were conducted on different samples. The first experiment was conducted by continuously collecting X-ray nano-tomography scans at one fixed location at  $700^\circ\text{C}$  using the sample made with the 0.3-mm quartz capillary. Secondly, a mosaic in situ tomography experiment was conducted by repeatedly taking mosaic tomography scans ( $3 \times 3 \times 1$ ,  $x \times y \times z$ ) during the in situ process to capture the morphological evolution of the full capillary, using the sample made with the 0.1-mm quartz capillary. The step size between each tomography was 25  $\mu\text{m}$ ; considering the horizontal field of view is 46.8  $\mu\text{m}$ , there was a 21.8- $\mu\text{m}$  overlap between the tomography volumes to enable adequate image stitching. The data were collected with an X-ray beam attenuator to mitigate the potential radiation damage. The mosaic tomography experiment included measurements at two distinct regions of the same sample, one with salt and one without salt (as a control experiment) in the sealed capillary, carried out consecutively.

After each heating experiment, the sample was cooled to room temperature with a ramp rate of  $50^\circ\text{C}/\text{min}$ . Tomography scans were collected prior to the heating and after the cooling of the samples. 2D TXM images were also collected during the heating and cooling process to record any potential morphological changes. In addition, 2D XANES imaging was also conducted at  $700^\circ\text{C}$  by scanning the Ni K-edge from 8.323 to 8.353 keV. Standards of Ni, NiO, and NiCl<sub>2</sub> were measured at room temperature. Additionally, for comparison, two Ni-20Cr (80 wt%Ni-20 wt% Cr) samples were studied by in situ heating TXM analysis at 700 and  $800^\circ\text{C}$ , respectively (see supplementary data file on the Methods for further details; refer to online supplementary material).

The tomographic projection images were reconstructed into volumetric images with the gridrec algorithm using Tomopy.<sup>52</sup> PyXAS<sup>53</sup> was used to process the XANES imaging data. The 3D images were stitched together to extend the imaging volume using Python programs developed in-house.<sup>54</sup> The 2D and 3D visualization was carried out by Fiji (a distribution of ImageJ with plug-ins for tomographic data processing)<sup>55</sup> and Avizo (Thermo Fisher Scientific, v9.3).

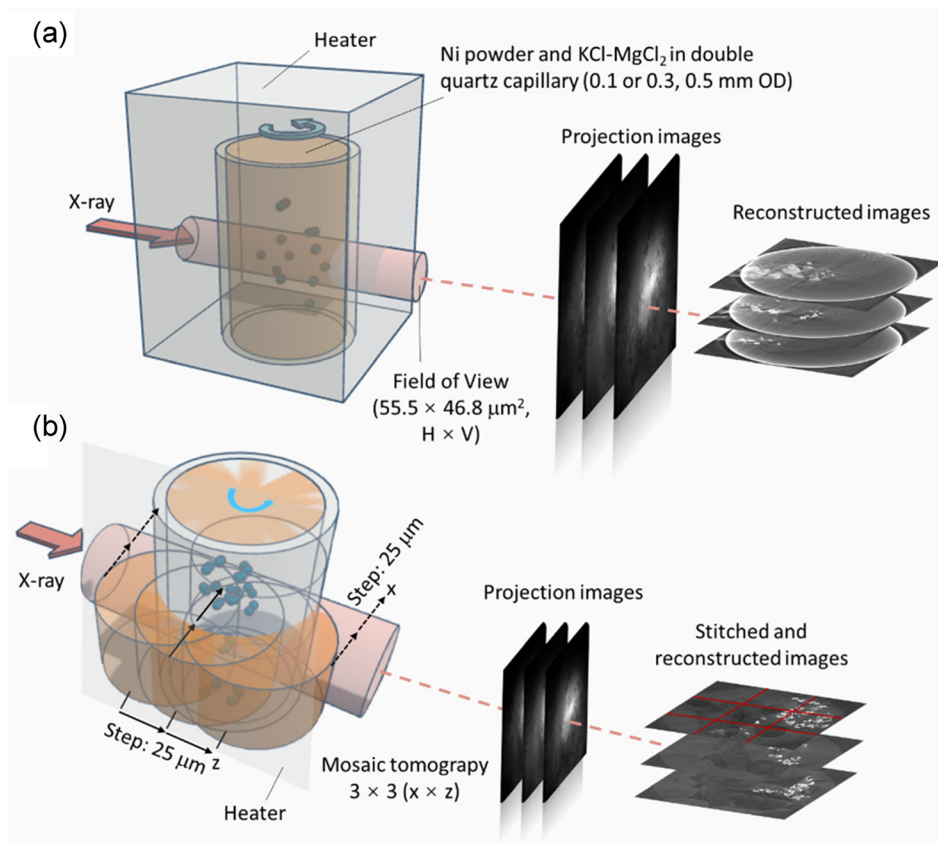


Fig. 1. In situ synchrotron X-ray nano-tomography experimental setup at 700°C to study the morphological evolution of Ni microparticles in KCl-MgCl<sub>2</sub>. Two experiments were carried out on two separate samples (the figures are not drawn to scale.): (a) continuous X-ray nano-tomography scans were taken at the same sample location in the first experiment; (b) the setup of the mosaic X-ray nano-tomography scans for the second experiment, conducted at two locations (with and without salt) within the same sample.

## RESULTS AND DISCUSSION

### The Initial Morphological Change of Ni Particles in Molten KCl-MgCl<sub>2</sub> Versus in Ar

With the rapid tomographic data collection at the FXI beamline, the very early stages (within  $\sim 3$  min) of the 3D morphological changes of the Ni particles were captured; the in situ heating experiments were conducted on the same sample in two different regions, one with Ni particles immersed in the molten salt environment and the other with Ni particles in a no-salt region. As shown in Fig. 2, the pristine Ni particles were mostly spherical and well dispersed in the salt, with a particle size  $\sim 2 \mu\text{m}$  in diameter. From the image contrast (Fig. 2a) and the pseudo-cross-sectional view in the *XY* plane (see supplementary Fig. S1), it could be identified that the particles were attached to the inner surface of the quartz capillary. After being heated in Ar at 700°C for 2.4 min, the particles started to connect together with a classic neck growth feature (see Fig. 2a, indicated with an orange arrow in the middle panel). With a continuous heating to 3.1 min, more particles became connected, but the particles did not fully merge, with neck features remaining clear between particles. This neck

growth phenomenon is commonly observed in sintering particles, a solid-state processing method typically carried out at a high temperature to convert powders into a structure with more mechanical integrity. The growth of the feature size in particles is driven by reducing the total interfacial area in order to lower the overall free energy of the system.<sup>28</sup>

For the particles submerged in molten salt, after being heated at 700°C for just 1.3 min (Fig. 2b), larger aggregates of particles were observed compared to the particles after 3.1 min in the Ar environment without the molten salt. The growth continued, as can be seen in the image from 2.9 min of heating. Previous work conducted by Zhang et al. has shown aggregation of nanocrystals (Pt) in molten AlCl<sub>3</sub>-NaCl-KCl.<sup>56</sup> In that study, the colloidal behavior of different nanocrystals including metals (Pt and Pd) was analyzed. The study demonstrates that stable colloids form only when there is a chemical affinity between the nanocrystals surface and the ions present in the molten salt. This shows that the salt composition, which changes its Lewis acidity, affects the reactivity and diffusivity at the metal surfaces. Combined with the observation of particle segregation of Ni in molten salts, these

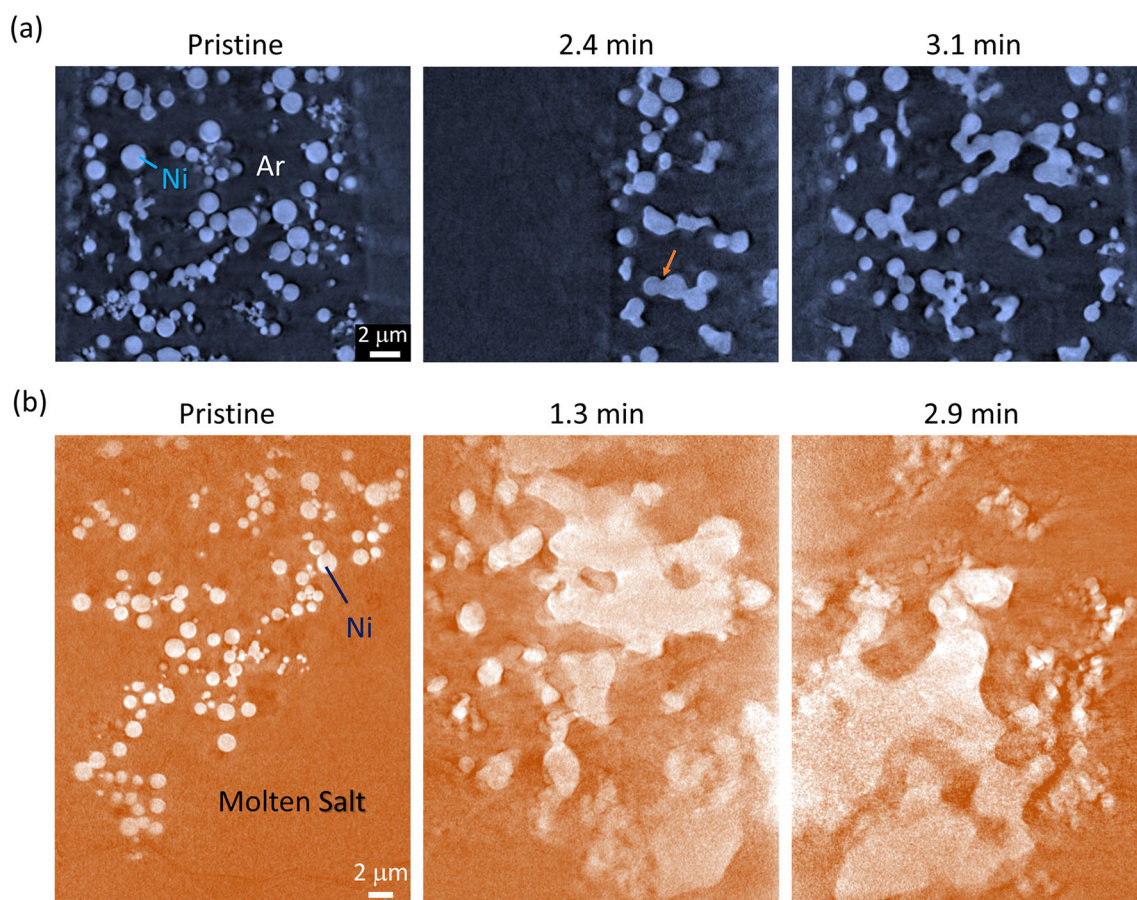


Fig. 2. The pseudocross-sectional view (XZ plane) from the X-ray nano-tomography reconstruction of the pristine Ni particles and their change in an Ar environment, as well as molten  $\text{KCl-MgCl}_2$  (50:50 mol%) at  $700^\circ\text{C}$ : (a) the morphological evolution of Ni particles in Ar; the orange arrow indicates the neck growth between particles from coarsening; (b) the morphological evolution of Ni particles in molten salt shows a much more rapid coarsening. Note that the images were not taken in the exactly the same region within the sample due to the particle motion (Color figure online).

observations should inspire future theoretical, experimental, and simulation work to study the behaviors of Ni and other structural elements (such as Cr and Fe) in different salt mixtures or compositions. The reactivity and diffusivity of the metals can vary in different salt mixtures, which may result in different morphological evolutions of alloys in molten salt. Overall, the image quality of the tomographic reconstruction from the molten salt region (Fig. 2b) was not as good as the one without the salt (Fig. 2a), which is consistent with the rapid change of the particles, likely accompanied by greater particle motion in the molten salt than in the Ar case. The growth of the Ni particles in molten salt could also be the result of mass transport between particles to reduce the interfacial area, similar to the behavior in coarsening and sintering processes. The large particles that formed in molten salt did not show the neck growth feature, which may be because the mass transport of Ni particles in the molten salt was much faster than without the molten salt, leading to a much more rapid particle growth. However, note that, due to the rapid feature size growth, there may be artifacts in the

reconstructed images, so the shapes of the features here should be viewed as a qualitative representation.

Additionally, the 3D morphological comparison of the pristine Ni particles, heated at  $700^\circ\text{C}$  in Ar for 2.4 min (see supplementary Video S1) and in molten salt for 1.3 min (see supplementary Video S2) are shown in Fig. 3a–c. In the large scale, many particles are connected by neck growth in Ar. In molten salt, the much more rapid growth and aggregates of large particles can be seen clearly in the 3D volume rendering view.

To confirm that the morphological evolution here is primarily due to mass transport leading to coarsening (possibly also densification), and not chemical reactions (e.g., oxide growth), the chemical states of the coarsened Ni particles in molten salt at  $700^\circ\text{C}$  were studied by 2D Ni K-edge XANES spectroscopic imaging, as shown in Fig. 4. Two regions of interest (ROIs) were selected on large particles formed in the molten salt (Fig. 4a). The averaged XANES spectra in the two regions are plotted in Fig. 4b, and compared with the Ni, NiO, and  $\text{NiCl}_2$  standards. The profiles and edge positions of the spectra in ROI-1 and ROI-2 are the

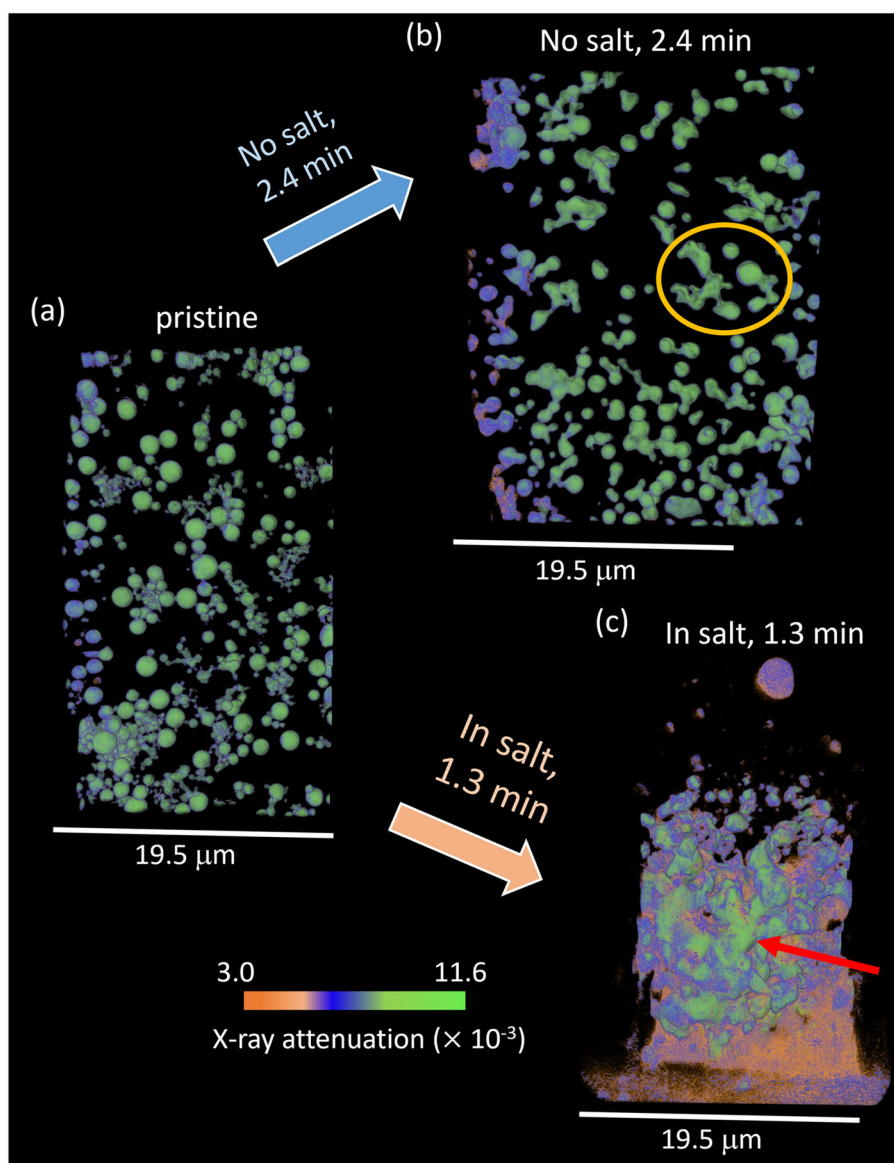


Fig. 3. The 3D visualization of the (a) pristine Ni particles; (b) the particle changes in Ar without molten salt for 2.4 min; and (c) the particle changes in molten  $\text{KCl-MgCl}_2$  for 1.3 min; the orange circle shows the coarsening of Ni particles with necking features, and the red arrow suggests the coarsened large Ni particles in molten salt (Color figure online).

same as the ones from the Ni standard. This shows that the large particles and aggregate structure formed in the molten salt are still fully metallic Ni. This supports the inference that there are no oxidation reactions contributing to the morphological changes in the Ni particles; this observation also further suggests that the rapid size increase of the Ni particles in molten salts was from mass transport.

The rapid Ni coarsening observed in the molten salt environment does not resemble the morphological evolution in classical coarsening (Ostwald ripening) or neck growth in sintering. While the exact mechanisms remain unclear, this rapid growth in the feature size suggests that the molten

salt can provide an alternative mass-transport pathway, and/or a faster diffusion rate, that are not available when the Ni is coarsening in Ar. Considering the mass transport mechanisms, in the salt, the long-range diffusion in liquids, and/or the surface diffusion along the solid-liquid (Ni-salt) interfaces, may be faster than the surface diffusion along the particles and/or the capillary walls in Ar. In addition, due to the presence of a temperature gradient along the vertical direction introduced by the heating elements, convection can drive particle movement within the molten salt. Furthermore, it is possible that some dissolution/redeposition process could take place. Future work will improve the

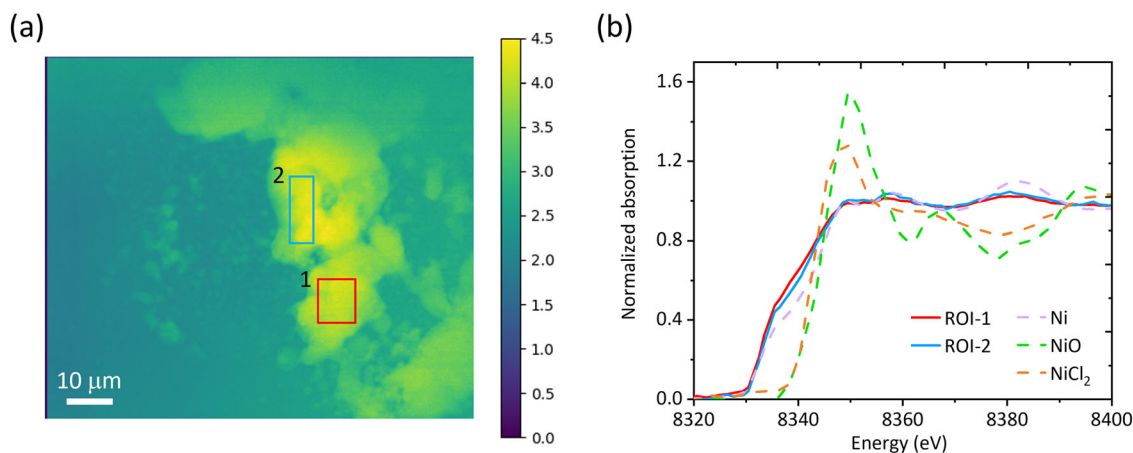


Fig. 4. The 2D XANES spectroscopic mapping on large Ni particles formed in the molten salt: (a) a representative frame of the 2D Ni K-edge XANES mapping with regions of interest (ROI-1 and 2); (b) normalized Ni K-edge XANES spectra of ROI-1 and ROI-2 with Ni, NiO, and NiCl<sub>2</sub> standards.

reconstruction image with quantitative analysis to study the kinetics of the morphological evolution of Ni in molten salt.

### The Heterogeneity of Morphological Evolution of Ni Particles in Molten Salts

In addition to the more rapid feature size growth of the Ni particles in molten salt, the study also revealed the heterogeneous morphological changes of Ni particles in molten salt. An in situ mosaic X-ray nano-tomography study was conducted, where the 3D volumes were stitched together to obtain a larger field of view. First, Fig. 5a shows the 2D projections from one tomographic measurement at two different rotation angles for a heating time ( $t$ ) of 35.5 min at 700°C. In addition to the growth of large Ni particles, there are many particles in the sub-micron or nanometer size ranges that are smaller than the pristine Ni particles in molten salt (indicated by a green rectangle in Fig. 5a). Future work can be conducted to use high-resolution scanning transmission electron microscopy (STEM) to study the size and formation of the particles. Furthermore, Fig. 5b shows the morphological evolution of the Ni particles in molten salt at different time points with pseudo-2D cross-sectional images from the in situ mosaic-tomography ( $XY$  plane views) experiment. Each image was stitched from a  $3 \times 3$  grid for a total of 9 tomographic measurements, in order to capture a full view of the capillary. The growth of the large particles (indicated by red arrows in Fig. 5b), as well as presence of many smaller, sub-micron/nanoparticles (indicated by green arrows in Fig. 5b) were observed. Similarly, there are some artifacts in the images, consistent with the fast motion and morphological evolution of the particles in molten salt; note that this issue was not observed for the sample heated only in an Ar environment. With the heating time of 79.8 min in molten salt, large Ni particles were observed. For

the particles heated in Ar at 700°C for a longer duration of 140.3 min (see supplementary Fig. S2), no comparable large Ni particles or sub-micron/nanoparticles were observed.

Because the mosaic tomography scans were taken during the in situ heating experiment to observe the overview, the time difference between two scans on a same location was long ( $\sim 7-9$  min), and it might be difficult to capture the dissolution of the Ni particles. Therefore, an in situ experiment with continuous tomographic data collection on the same location was conducted, in which the dissolution of the Ni particles was observed (Fig. 6). The red arrows in Fig. 6 indicate the regions that show the dissolution of Ni particles in the molten salt. The dissolution of Ni would imply that there is an oxidation of metallic solid Ni into Ni<sup>2+</sup> (ions dissolved in the molten salt).<sup>57</sup> The oxidation of Ni would likely be driven by the trace amounts of impurities in the salt.<sup>15</sup> Although purified KCl-MgCl<sub>2</sub> was used in this work, such trace amounts of impurities (H<sub>2</sub>O, O<sub>2</sub> and MgOHCl) could be introduced into the sample during sample preparation. The Ni K-edge XANES spectra from the salt region of the sample measured in the mosaic tomography experiment are noisy, likely due to limited Ni dissolution into the molten salt, and thus one cannot determine the exact chemical form of the Ni species in the salt region (see supplementary Fig. S3). However, the presence of an edge jump across the Ni K-edge indicates that there are indeed Ni-containing species in the molten salt, but their concentration is low. Further studies will be needed to understand the chemical states of Ni. Similar to the other experimental results presented in Figs. 2, 3, 4, and 5), here, many nanoparticles are identified in this in situ sample. In addition, the experiment showed a similar rapid coarsening, although the morphological evolution seems to conform with the classical coarsening model (see supplementary Fig. S4).

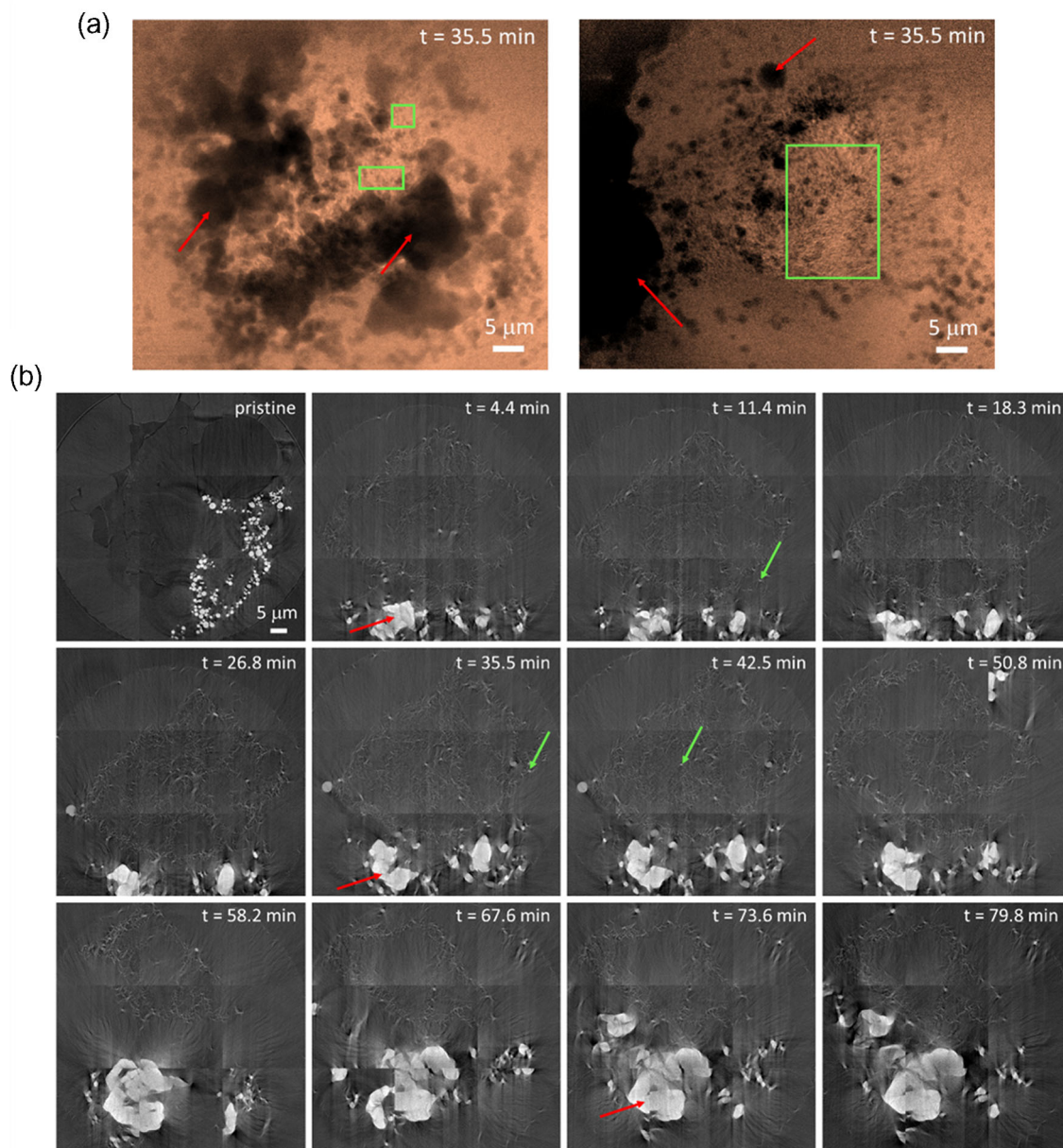


Fig. 5. The morphological evolution of Ni particles in molten  $\text{KCl-MgCl}_2$  at  $700^\circ\text{C}$ : (a) 2D projections at 35.5 min with different rotation angles showing the large particles and nanoparticles dispersed in the molten salt; (b) assembled 2D mosaic XY images at selected time points showing the real-time change of particles in molten salt in a large field of view; red arrows in (a) and (b) show the large agglomeration of particles, and green rectangles in (a) and green arrows in (b) highlight small particles (Color figure online).

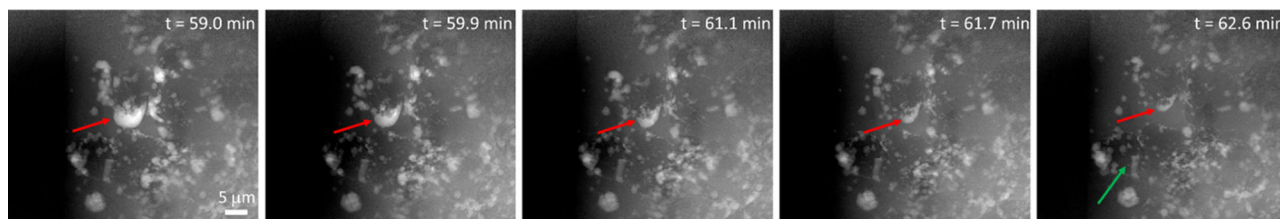


Fig. 6. 2D projections of the Ni particles in molten salt at selected time points showing the dissolution of Ni particles (red arrows) and the green arrow (Color figure online).



Note that this continuous nano-tomography experiment was conducted on the same region repeatedly, without adding an X-ray attenuator (see Methods for more details). Thus, the local region is likely receiving a higher X-ray dose compared to the other experiment. Here, several complex effects are worth noting. In addition to the prior discussions on the thermal gradient leading to convection, locally the amount of salt and the concentration of the Ni particles can vary, leading to a more heterogeneous morphology compared with the prior experiment. The ionizing radiation effects of the X-ray beam also have an impact, as observed previously in related studies.<sup>49</sup> In particular, bubble formation was observed during the imaging, as shown in supplementary Fig. S5. Interestingly, bubbles were seen in the projection images, where some particles were at the interface of the molten salt and the bubble. The bubbles from Ar trapped in the pristine sample, or gas produced from the corrosion reaction. Supplementary Video S3 shows how another sample was also changing during the heating process. Bubbles were observed during the heating process.

These factors contribute to the overall morphological heterogeneity observed in the current

measurements. For instance, in some regions, dissolution of Ni particles was observed instead of significant coarsening as observed in other locations (Fig. 5). This observation supports the explanation that the smaller, well-dispersed particles observed in Figs. 5 and 7 may simply be due to the dissolution of the original Ni microparticles. Note that the data in Fig. 5 were taken at 700°C, while Fig. 7 was based on data collected after the sample was cooled to room temperature. The particles were tracked via X-ray microscopy; however, the particles in these figures may be different due to the motion of the particles. However, it was unclear why these particles do not coarsen or aggregate like the pristine Ni particles. The morphological heterogeneity attributed to the complexity of the system should be further analyzed, particularly to better understand the kinetics (rate and pathways) of the various mechanisms, as well as the dynamical balance of the system in equilibrium. For instance, the concurrence of dissolution and deposition can be discussed, as well as the effects from local gradients in salt–metal concentration and temperature, that together drive the varying degrees of the growth and dissolution in different regions.

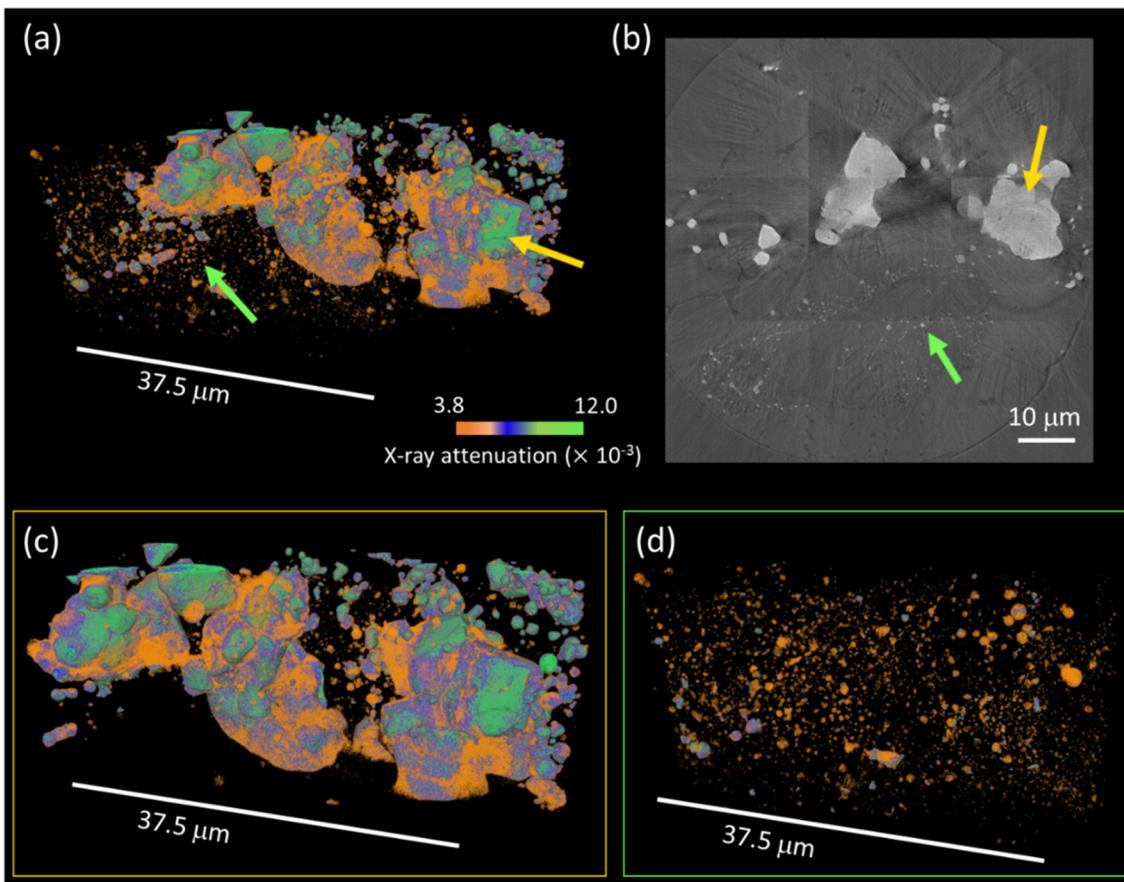


Fig. 7. The morphology of the Ni particles in molten salt after cooling to room temperature: (a) overview of the 3D morphology of the sample; (b) pseudo-2D XY view; (c) detailed 3D visualization of the large particles; (d) detailed 3D visualization of the nanoparticles formed in molten salt; yellow arrows indicate large particles and green arrows indicate the nanoparticles (Color figure online).

This morphological heterogeneity can be observed well in samples after an *operando* heating experiment. After cooling the in situ sample to room temperature, another mosaic tomography set was collected on the solidified sample. Figure 7 shows the visualization of the cooled sample, where Fig. 7c, d shows the detailed 3D views of the large Ni particle and smaller, sub-micron/nanoparticles extracted from Fig. 7a (see supplementary Fig. S6). Both the larger and smaller particles were preserved during the cooling process (see supplementary Video S4). Here, the formation mechanism of the nanoparticles will be further discussed. First, the XANES spectra shows that the chemical state of the small particles is still metallic Ni (see supplementary Fig. S7). Thus, the observed nanoparticles are not products of the chemical oxidation and precipitation of NiO or NiCl<sub>2</sub>.

As a comparison, nanoparticle formation was clearly observed from the reaction of Ni-20Cr microwires (80–20 wt.%) in molten KCl-MgCl<sub>2</sub> (50:50 mol%) at 500°C in 20 s.<sup>42</sup> The elemental analysis from STEM with energy-dispersive X-ray spectroscopy in our prior work<sup>42</sup> showed that there were Ni-rich particles in the corroded sample, which were likely from the detachment of material from reacted Ni-20Cr. Supplementary Videos S5 and S6 shows the emergence and growth of the nanoparticles during Ni-20Cr corrosion in molten KCl-MgCl<sub>2</sub> during in situ heating processes at 700 and 800°C, respectively. Furthermore, supplementary Video S7 shows the dissolution of the formed nanoparticles at 800°C. Note that the formation of these nanoparticles from Ni-20Cr in molten salt was observed as a parasitic event to the main corrosion and dealloying processes; the combination of the ionizing radiation from X-rays and molten salts likely plays a role, but the exact mechanism remains unclear. The connections between these nanoparticles as shown in the supplementary Videos S5–S7 and the detached particles identified by STEM/EDX in our prior work are also unclear. Thus, further work will be needed to systematically analyze the formation of the nanoparticles in similar conditions of Ni-20Cr and other metals/alloys under radiation effects to better understand the mechanisms.

Due to the spatial and time resolution limitations, it is unclear whether the nanoparticles observed in the Ni-particle experiment were also from nanoparticle formation similar to the Ni-20Cr experiments. One possible formation mechanism for the nanoparticles could be the fast break up or dissolution of the micron-sized pristine or coarsened Ni particles. Although purified salt was used, trace amounts of oxidant impurities could still be present in the system, due to the hygroscopic nature of MgCl<sub>2</sub> or sample manipulation. Ni could be oxidized into molten salt as Ni<sup>2+</sup> until reaching the solubility limit of NiCl<sub>2</sub> or completely consuming the residual oxidants. Moreover, Dias et al. reported Ni nanoparticle (~1.0 nm diameter)

formation under a synchrotron X-ray beam for 0.05–1.0 wt.% NiCl<sub>2</sub> in molten ZnCl<sub>2</sub> at 320°C, with 10–20 min beam exposure, by X-ray absorption spectroscopy measurements; their study showed that excess electrons produced by X-ray irradiation of ZnCl<sub>2</sub> leads to a reduction of Ni<sup>2+</sup> and Ni nanoparticle formation.<sup>49</sup> Since the dissolution of Ni was observed, there should be Ni<sup>2+</sup> ions in the molten salt. The dominant behavior of Ni observed in this study is aggregation and coarsening. The dissolution of Ni was local, because the purified salt contains only trace amounts of impurities, which can cause corrosion. Another possibility for no obvious Ni<sup>2+</sup> in the salt is that X-rays may induce reduction on Ni<sup>2+</sup>, as reported in the literature.<sup>49</sup>

## CONCLUSION

The aim of this work is to fundamentally understand Ni behavior in molten salt because of the application of Ni-based alloys in molten salt reactors. While much work has been carried out on engineering alloys, there remains a lack of understanding on the fundamental mechanisms of how metals interact with molten salts. This work examined the morphological evolution of Ni particles, including coarsening, dissolution, and nanoparticle formation, in molten KCl-MgCl<sub>2</sub> by in situ synchrotron X-ray nano-tomography. Faster growth and agglomeration of the Ni particles was observed in the molten salt compared to the Ar environment. The large Ni particles produced did not show a classical neck-growth feature nor a typical morphological evolution as in Ostwald ripening. However, the chemical states of these large Ni particles, characterized by XANES imaging, remain as metallic Ni, suggesting that this feature size growth is due to mass transport mechanisms and not oxidation reactions. In addition, smaller metallic Ni sub-micron/nanoparticles were formed, and were found to be relatively stable in molten salt. The nanoparticles may be from the dissolution or breakage of large Ni particles or they could be formed by the reduction of dissolved Ni ions by X-ray radiation. Note that coarsening and dissolution of Ni can occur concurrently in molten salt and thus may exhibit a dynamic balance and/or competition between the two mechanisms. Future work by in situ X-ray diffraction, X-ray absorption spectroscopy, or transmission electron microscopy needs to be conducted to further understand the nanoparticle formation in molten salt.

Overall, this work provides a direct observation on the morphological evolution of Ni, including coarsening/agglomeration and dissolution behaviors, in molten salt compared to an environment without the salt. The heterogeneous environment of the molten salt and alloy system, such as temperature gradients and radiation effects, will result in different reaction mechanisms being favored in

different parts of the reactor system. Future studies need to be conducted to understand the effects of individual parameters and their cross-coupling effects in determining the behavior of metals in contact with molten salt. Such an analysis may be extended to other metal elements used in molten salt applications, which have different chemical reactivities in molten salt, as well as different transport properties. It may be possible to also differentiate the effects of the radiation and temperature by analyzing samples heat-treated ex situ without the exposure to X-ray beams. It is important, however, to ensure that the cooling process does not significantly alter the morphology and chemistry of the samples. Using complementary characterization techniques with different interaction mechanisms (diffraction, spectroscopy, and imaging) and X-ray radiation dose density (local versus bulk probes) as a multimodal approach will also enable cross-checking the phenomena occurring in the samples. Future work, where *operando* X-ray nano-tomography experiments can be combined with in situ X-ray diffraction, X-ray absorption spectroscopy, and transmission electron microscopy, to better understand the correlation between the morphological, chemical, and structural changes, will be invaluable.

## SUPPLEMENTARY INFORMATION

The online version contains supplementary material available at <https://doi.org/10.1007/s11837-023-05715-8>.

## ACKNOWLEDGEMENTS

This work was supported as part of the Molten Salts in Extreme Environments (MSEE) Energy Frontier Research Center, funded by the U.S. Department of Energy, Office of Science, Basic Energy Sciences. BNL and ORNL are operated under DOE Contracts DE-SC0012704, and DE-AC05-00OR22725, respectively. Work at Stony Brook University was supported by MSEE through a subcontract from BNL. This research used resources and the Full Field X-ray Imaging (FXI, 18-ID) beamline of the National Synchrotron Light Source II, a U.S. Department of Energy (DOE) Office of Science User Facility operated for the DOE Office of Science by Brookhaven National Laboratory under Contract DE-SC0012704. We thank Dr. James Wishart, Dr. Simon Pimblott, Prof. Katsuyo Thornton, Prof. Adrien Couet, and Prof. Anatoly Frenkel for helpful discussions as part of the MSEE activities, as well as their great insights contributing to the interpretation and future work planning mentioned in this manuscript. We thank Bobby Layne for helping with the heater and experimental setup. Current and former Chen-

Wiegart group members are acknowledged for helping the beamtime: Xiaoyin Zheng, Varun Ravi Kankanallu, Charles Clark, and Cheng-Chu Chung.

## FUNDING

Funding was provided by the U.S. Department of Energy Office of Science, Office of Basic Energy Sciences under contracts DE-SC0012704 and DE-AC05-00OR22725.

## DATA AVAILABILITY STATEMENT

The digital data for all figures, tables, charts, and any other media contained in this publication and its associated supporting information files will be made accessible on the journal website (a publicly available site), and also on the Zenodo repository, under Digital Object Identifier <https://doi.org/10.5281/zenodo.7037700>.

## DECLARATIONS

## CONFLICT OF INTEREST

The authors declare that they have no conflict of interest.

## REFERENCES

1. S. Roy, Y. Liu, M. Topsakal, E. Dias, R. Gakhar, W.C. Phillips, J.F. Wishart, D. Leshchev, P. Halstenberg, S. Dai, S.K. Gill, A.I. Frenkel, and V.S. Bryantsev, *J. Am. Chem. Soc.* 143, 15298–15308. <https://doi.org/10.1021/jacs.1c06742> (2021).
2. T.R.A. K. Sridharan, *Molten Salts Chemistry*, in edited by H.G. F. Lantelme (Elsevier, 2013), pp 241-267.
3. S.S. Raiman and S. Lee, *J. Nucl. Mater.* 511, 523–535. <https://doi.org/10.1016/j.jnucmat.2018.07.036> (2018).
4. W.J. Ding, H. Shi, A. Jianu, Y.L. Xiu, A. Bonk, A. Weisenburger, and T. Bauer, *Sol. Energy Mater. Sol. Cells* 193, 298–313. <https://doi.org/10.1016/j.solmat.2018.12.020> (2019).
5. S. Bell, T. Steinberg, and G. Will, *Renew. Sustain. Energy Rev.* 114, 109328. <https://doi.org/10.1016/j.rser.2019.109328> (2019).
6. A.G. Fernandez, J. Gomez-Vidal, E. Oro, A. Kruiženga, A. Sole, and L.F. Cabeza, *Renew. Energy* 140, 152–176. <https://doi.org/10.1016/j.renene.2019.03.049> (2019).
7. M. Mehos, C. Turchi, J. Vidal, M. Wagner, Z. Ma, C. Ho, W. Kolb, C. Andraka, A. Kruiženga, Report No. NREL/TP-5500-674642017.
8. M. Lambrecht, M.T. de Miguel, M.I. Lasanta, and F.J. Perez, *Sol. Energy Mater. Sol. Cells*. <https://doi.org/10.1016/j.solmat.2021.111557> (2022).
9. N. Klammer, C. Engtrakul, Y.Y. Zhao, Y.L. Wu, and J. Vidal, *Anal. Chem.* 92, 3598–3604. <https://doi.org/10.1021/acs.analchem.9b04301> (2020).
10. Q. Pang, J. Meng, S. Gupta, X. Hong, C.Y. Kwok, J. Zhao, Y. Jin, L. Xu, O. Karahan, Z. Wang, and S. Toll, *Nature* 608, 704–711. <https://doi.org/10.1038/s41586-022-04983-9> (2022).
11. H.Y. Yin, B. Chung, F. Chen, T. Ouchi, J. Zhao, N. Tanaka, and D.R. Sadoway, *Nat. Energy* 3, 127–131. <https://doi.org/10.1038/s41560-017-0072-1> (2018).
12. L. Xu, B. Wang, F.S. Han, S.Y. Liu, P. Sheng, H. Li, G.Y. Zhao, X. Chen, H.T. Bai, T.T. Li, and C. He, *Chem. Phys. Lett.* <https://doi.org/10.1016/j.cplett.2020.137210> (2020).
13. M.M. Li, X.W. Zhan, E. Polikarpov, N.L. Canfield, M.H. Engelhard, J.M. Weller, D.M. Reed, V.L. Sprenkle, and G.S.

- Li, *Cell Rep. Phys. Sci.* <https://doi.org/10.1016/j.xcrp.2022.100821> (2022).
14. R.O. Scarlat, M.R. Laufer, E.D. Blandford, N. Zweibaum, D.L. Krumwiede, A.T. Cisneros, C. Andreades, C.W. Forsberg, E. Greenspan, L.W. Hu, P.F. Peterson, *Design and licensing strategies for the fluoride-salt-cooled, high-temperature reactor (FHR) technology*, (2014).
15. A. Ronne, L.F. He, D. Dolzhenkov, Y. Xie, M.Y. Ge, P. Halstenberg, Y.C. Wang, B.T. Manard, X.H. Xiao, W.K. Lee, K. Sasaki, S. Dai, S.M. Mahurin, Y.C.K. Chen-Wiegart, and A.C.S. Appl. Mater. Interf. 12, 17321–17333. <https://doi.org/10.1021/acsami.9b19099> (2020).
16. J. Serp, M. Allibert, O. Benes, S. Delpech, O. Feynberg, V. Ghetta, D. Heuer, D. Holcomb, V. Ignatiev, J.L. Kloosterman, L. Luzzi, E. Merle-Lucotte, J. Uhlir, R. Yoshioka, and Z.M. Dai, *Prog. Nucl. Energy* 77, 308–319. <https://doi.org/10.1016/j.pnucene.2014.02.014> (2014).
17. S.K. Gupta and Y.B. Mao, *J. Phys. Chem. C* 125, 6508–6533. <https://doi.org/10.1021/acs.jpcc.0c10981> (2021).
18. V. Kamysbayev, A.S. Filatov, H.C. Hu, X. Rui, F. Lagunas, D. Wang, R.F. Klie, and D.V. Talapin, *Science* 369, 979. <https://doi.org/10.1126/science.aba8311> (2020).
19. Y.B. Li, H. Shao, Z.F. Lin, J. Lu, L.Y. Liu, B. Duployer, P.O.A. Persson, P. Eklund, L. Hultman, M. Li, K. Chen, X.H. Zha, S.Y. Du, P. Rozier, Z.F. Chai, E. Raymundo-Pinero, P.L. Taberna, P. Simon, and Q. Huang, *Nat. Mater.* 20, 571–571. <https://doi.org/10.1038/s41563-021-00925-4> (2021).
20. S.Q. Guo, J.S. Zhang, W. Wu, and W.T. Zhou, *Prog. Mater. Sci.* 97, 448–487. <https://doi.org/10.1016/j.pmatsci.2018.05.003> (2018).
21. R. Chesser, S.Q. Guo, and J.S. Zhang, *Fuel Cycle and Waste Management*, vol. 116 (2017), pp. 155–157. <https://www.ans.org/pubs/transactions/article-40548/>.
22. D. Sulejmanovic, J.M. Kurlay, K. Robb, and S. Raiman, *J. Nucl. Mater.* <https://doi.org/10.1016/j.jnucmat.2021.152972> (2021).
23. G.Q. Zheng, L.F. He, D. Carpenter, and K. Sridharan, *J. Nucl. Mater.* 482, 147–155. <https://doi.org/10.1016/j.jnucmat.2016.10.023> (2016).
24. H. Sun, J.Q. Wang, Z.F. Tang, Y.Y. Liu, and C.Y. Wang, *Corros. Sci.* <https://doi.org/10.1016/j.corsci.2019.108350> (2020).
25. W.Y. Zhou, Y. Yang, G.Q. Zheng, K.B. Woller, P.W. Stahle, A.M. Minor, and M.P. Short, *Nat. Commun.* <https://doi.org/10.1038/s41467-020-17244-y> (2020).
26. S.Q. Guo, W.Q. Zhuo, Y.F. Wang, and J.S. Zhang, *Corros. Sci.* <https://doi.org/10.1016/j.corsci.2019.108279> (2020).
27. L.L. Guo, Q. Liu, H.Q. Yin, T.J. Pan, and Z.F. Tang, *Corros. Sci.* 166, 108473. <https://doi.org/10.1016/j.corsci.2020.108473> (2020).
28. R.W. Balluffi, S.M. Allen, and W. Craig Carter, *Kinetics of Materials* (Wiley, New York, 2005).
29. P.W.V. Lorenz Ratke, *Growth and Coarsening: Ostwald Ripening in Material Processing* (Springer, Berlin, 2002).
30. X.Y. Liu, A. Ronne, L.C. Yu, Y. Liu, M.Y. Ge, C.H. Lin, B. Layne, P. Halstenberg, D.S. Maltsev, A.S. Ivanov, S. Antonelli, S. Dai, W.K. Lee, S.M. Mahurin, A.I. Frenkel, J.F. Wishart, X.H. Xiao, and Y. Chen-Wiegart, *Nat. Commun.* <https://doi.org/10.1038/s41467-021-23598-8> (2021).
31. T. Ghaznavi, S.Y. Persaud, and R.C. Newman, *J. Electrochem. Soc.* <https://doi.org/10.1149/1945-7111/ac735b> (2022).
32. T. Ghaznavi, M.A. Bryk, S.Y. Persaud, and R.C. Newman, *Corros. Sci.* <https://doi.org/10.1016/j.corsci.2021.110003> (2022).
33. Y.C.K. Chen-Wiegart, S. Wang, Y.S. Chu, W.J. Liu, I. McNulty, P.W. Voorhees, and D.C. Dunand, *Acta Mater.* 60, 4972–4981. <https://doi.org/10.1016/j.actamat.2012.05.012> (2012).
34. W.B. Andrews, K.L.M. Elder, P.W. Voorhees, and K. Thornton, *Phys. Rev. Mater.* 4, 103401. <https://doi.org/10.1103/PhysRevMaterials.4.103401> (2020).
35. Y.C.K. Chen, Y.S. Chu, J. Yi, I. McNulty, Q. Shen, P.W. Voorhees, and D.C. Dunand, *Appl. Phys. Lett.* <https://doi.org/10.1063/1.3285175> (2010).
36. C.H. Zhao, T. Wada, V. De Andrade, G.J. Williams, J. Gelb, L. Li, J. Thieme, H. Kato, Y.C.K. Chen-Wiegart, and A.C.S. Appl. Mater. Interf. 9, 34172–34184. <https://doi.org/10.1021/acsami.7b04659> (2017).
37. L.J. Zou, M.Y. Ge, C.H. Zhao, Q.K. Meng, H. Wang, X.Y. Liu, C.H. Lin, X.H. Xiao, W.K. Lee, Q. Shen, F. Chen, Y.C.K. Chen-Wiegart, and A.C.S. Appl. Mater. Interf. 12, 2793–2804. <https://doi.org/10.1021/acsami.9b16392> (2020).
38. G.B. Zan, G.N. Qian, S. Gul, H.Y. Pan, Q. Li, J.Z. Li, D.J. Vine, S. Lewis, W.B. Yun, P. Pianetta, H. Li, X.Q. Yu, Y.J. Liu, and A.C.S. Mater. Lett. 3, 1786–1792. <https://doi.org/10.1021/acsmaterialslett.1c00600> (2021).
39. Y.Q. Wang, J.R. Gao, W.H. Sun, and A.J. Shahani, *Scr. Mater.* <https://doi.org/10.1016/j.scriptamat.2021.114224> (2022).
40. M.B. Kelly, S. Niverty, and N. Chawla, *Acta Mater.* 189, 118–128. <https://doi.org/10.1016/j.actamat.2020.02.052> (2020).
41. Y.C. Lin, X.Y. Liu, K.W. Chou, E.H.R. Tsai, C.H. Zhao, M. Holler, A. Diaz, S. Petrash, and Y.C.K. Chen-Wiegart, *Adv. Eng. Mater.* 22, 1901250. <https://doi.org/10.1002/adem.201901250> (2020).
42. K. Bawane, X.Y. Liu, R. Gakhar, M. Woods, M.Y. Ge, X.H. Xiao, W.K. Lee, P. Halstenberg, S. Dai, S. Mahurin, S.M. Pimblott, J.F. Wishart, Y.C.K. Chen-Wiegart, and L.F. He, *Corros. Sci.* <https://doi.org/10.1016/j.corsci.2021.109962> (2022).
43. J.R. Wilson, W. Kobsiriphat, R. Mendoza, H.Y. Chen, J.M. Hiller, D.J. Miller, K. Thornton, P.W. Voorhees, S.B. Adler, and S.A. Barnett, *Nat. Mater.* 5, 541–544. <https://doi.org/10.1038/nmat1668> (2006).
44. H.Y. Chen, H.C. Yu, J.S. Cronin, J.R. Wilson, S.A. Barnett, and K. Thornton, *J. Power Sourc.* 196, 1333–1337. <https://doi.org/10.1016/j.jpowsour.2010.08.010> (2011).
45. M. Trini, S. De Angelis, P.S. Jorgensen, P.V. Hendriksen, K. Thornton, and M. Chen, *Acta Mater.* <https://doi.org/10.1016/j.actamat.2021.116887> (2021).
46. K.L.M. Elder, W.B. Andrews, M. Ziehmer, N. Mameka, C. Kirchlechner, A. Davydok, J.S. Micha, A.F. Chadwick, E.T. Lilleodden, K. Thornton, and P.W. Voorhees, *Proc. Natl. Acad. Sci. U. S. A.* <https://doi.org/10.1073/pnas.2104132118> (2021).
47. Y.C.K. Chen-Wiegart, W.M. Harris, J.J. Lombardo, W.K.S. Chiu, and J. Wang, *Appl. Phys. Lett.* <https://doi.org/10.1063/1.4772784> (2012).
48. S.F. Li, Z.S. Jiang, J.X. Han, Z.R. Xu, C.X. Wang, H. Huang, C. Yu, S.J. Lee, P. Pianetta, H. Ohldag, J.S. Qiu, J.S. Lee, F. Lin, K.J. Zhao, and Y.J. Liu, *Nat. Commun.* <https://doi.org/10.1038/s41467-020-18278-y> (2020).
49. E.T. Dias, S.K. Gill, Y. Liu, P. Halstenberg, S. Dai, J.H. Huang, J. Mausz, R. Gakhar, W.C. Phillips, S. Mahurin, S.M. Pimblott, J.F. Wishart, and A.I. Frenkel, *J. Phys. Chem. Lett.* 12, 157–164. <https://doi.org/10.1021/acs.jpcclett.0c03231> (2021).
50. M.Y. Ge, D.S. Coburn, E. Nazaretski, W.H. Xu, K. Gofron, H.J. Xu, Z.J. Yin, and W.K. Lee, *Appl. Phys. Lett.* 113, 083109. <https://doi.org/10.1063/1.5048378> (2018).
51. S. Antonelli, A. Ronne, I. Han, M.Y. Ge, B. Layne, A.J. Shahani, K. Iwamatsu, J.F. Wishart, S.L. Hulbert, W.K. Lee, Y.C.K. Chen-Wiegart, and X.H. Xiao, *J. Synchrotron Radiat.* 27, 746–752. <https://doi.org/10.1107/s1600577520004567> (2020).
52. D. Gursoy, F. De Carlo, X.H. Xiao, and C. Jacobsen, *J. Synchrotron Radiat.* 21, 1188–1193. <https://doi.org/10.1107/s1600577514013939> (2014).
53. M.Y. Ge and W.K. Lee, *J. Synchrotron Radiat.* 27, 567–575. <https://doi.org/10.1107/s1600577520001071> (2020).
54. C.H. Lin, Z.Y. Ju, X.Y. Zheng, X. Zhang, N. Zmich, X.Y. Liu, K.J. Takeuchi, A.C. Marschilok, E.S. Takeuchi, M.Y. Ge, G.H. Yu, and Y.C.K. Chen-Wiegart, *Carbon* 188, 114–125. <https://doi.org/10.1016/j.carbon.2021.11.014> (2022).

55. C.T. Rueden, J. Schindelin, M.C. Hiner, B.E. DeZonia, A.E. Walter, E.T. Arena, and K.W. Eliceiri, *BMC Bioinf.* <https://doi.org/10.1186/s12859-017-1934-z> (2017).
56. H. Zhang, K. Dasbiswas, N.B. Ludwig, G. Han, B. Lee, S. Vaikuntanathan, and D.V. Talapin, *Nature* 542, 328. <https://doi.org/10.1038/nature21041> (2017).
57. K. Bawane, P. Manganaris, Y.C. Wang, J. Sure, A. Ronne, P. Halstenberg, S. Dai, S.K. Gill, K. Sasaki, Y.C.K. Chen-Wiegart, R. Gakhar, S. Mahurin, S.M. Pimblott, J.F. Wishart, and L.F. He, *Scr. Mater.* <https://doi.org/10.1016/j.scriptamat.2021.113790> (2021).

**Publisher's Note** Springer Nature remains neutral with regard to jurisdictional claims in published maps and institutional affiliations.

Springer Nature or its licensor (e.g. a society or other partner) holds exclusive rights to this article under a publishing agreement with the author(s) or other rightsholder(s); author self-archiving of the accepted manuscript version of this article is solely governed by the terms of such publishing agreement and applicable law.